nature energy

ARTICLES

https://doi.org/10.1038/s41560-019-0402-6

Atomically dispersed platinum supported on curved carbon supports for efficient electrocatalytic hydrogen evolution

Daobin Liu[1,6], Xiyu Li[2,6], Shuangming Chen[1], Huan Yan[2], Changda Wang[1], Chuanqiang Wu[1], Yasir A. Haleem[1], Sai Duan[3], Junling Lu[2], Binghui Ge[4], Pulickel M. Ajayan[5], Yi Luo[2], Jun Jiang[2*] and Li Song[1*]

Dispersing catalytically active metals as single atoms on supports represents the ultimate in metal utilization efficiency and is increasingly being used as a strategy to design hydrogen evolution reaction (HER) electrocatalysts. Although platinum (Pt) is highly active for HER, given its high cost it is desirable to find ways to improve performance further while minimizing the Pt loading. Here, we use onion-like nanospheres of carbon (OLC) to anchor stable atomically dispersed Pt to act as a catalyst (Pt_1/OLC) for the HER. In acidic media, the performance of the Pt_1/OLC catalyst (0.27 wt% Pt) in terms of a low overpotential (38 mV at 10 mA cm^{-2}) and high turnover frequencies (40.78 H_2 s^{-1} at 100 mV) is better than that of a graphene-supported single-atom catalyst with a similar Pt loading, and comparable to a commercial Pt/C catalyst with 20 wt% Pt. First-principle calculations suggest that a tip-enhanced local electric field at the Pt site on the curved support promotes the reaction kinetics for hydrogen evolution.

The nature, size, placement and stability of metallic particles can have a strong influence on their activity in catalytic reactions[1–3]. Reducing the size of the metal catalysts to very small particles on supports is an efficient approach to expose more catalytic active sites[4–6] as it maximizes the amount of the catalytically active species within the limited surface area[3]. The ultimate in metal utilization is to engineer single metal atoms on appropriate supports[7–11], which not only reduces the overall metal loading needed for catalysis, but also improves the efficiency and selectivity of reactions because the low coordination nature of a single metal atom potentially induces high chemical activities, as long as these sites can be rendered active for extended durations[12,13].

The electrochemical hydrogen evolution reaction (HER) is a fundamental step in water splitting and can realize the highly efficient energy conversion and storage from the intermittent sources (for example, wind or solar)[1,14]. Platinum (Pt) is the most efficient component to trigger the HER with a minimum overpotential and fast kinetics owing to its favourable hydrogen binding energy[14]. However, the high cost and natural scarcity of Pt limit its large-scale use[1,13]. In this regard, several attempts have been successfully made to prepare Pt-based single-atom catalysts (SACs)[15–17] to minimize the amount of Pt metal required to catalyse the HER efficiently, but the activity still has much room for improvement.

As is known, the corner and edge sites of catalysts often possess a superior activity[3]. Inspired by this, we set out to utilize highly curved supports to anchor single metal sites with a view to mimicking metal sites at the corners and edges of particles. Here, we demonstrate that the distribution of Pt single atoms on nanosized onion-like carbon (OLC) supports (Pt_1/OLC) can produce highly efficient electrocatalysts for hydrogen evolution, where the activity outperforms that of a two-dimensional (2D) graphene-supported catalyst at a similar Pt loading. Simulations suggest that this architecture with a high curvature leads to the accumulation of electrons around the Pt regions, which induces a local electric field and accelerates the catalytic kinetics.

Synthesis of Pt single atoms on curved carbon supports

To realize this ingenious catalyst design (Fig. 1a), to engineer vacancy defects and functional groups on the OLC supports is a critical step to stabilize isolated metal atoms[7,9,18,19]. In our experiments, surface-oxidized detonation nanodiamonds (DNDs) were selected as the starting material to obtain OLC due to their near uniform small-size distribution. This material was treated via thermal deoxygenation at various temperatures to tune precisely the type and distribution density of oxygen species, and the DND was automatically transformed into an OLC at elevated temperatures (>900 °C) (Supplementary Figs. 1 and 2)[20]. Then, a single cycle atomic layer deposition (ALD) was used to produce isolated Pt atoms on all the supports.

To identify the form of the Pt atoms distributed on OLC supports, high-angle annular dark-field scanning transmission electron microscopy (HAADF-STEM) was used. It is shown in Fig. 1b (more images in Supplementary Fig. 3) that isolated Pt atoms (named as Pt_1/OLC) were observed all over the support with no obvious nanoparticles or clusters present. Meanwhile, typical multishell fullerene structures of diameter ~5 nm and with interlayer distances

[1]National Synchrotron Radiation Laboratory, CAS Center for Excellence in Nanoscience, University of Science and Technology of China, Hefei, China. [2]Hefei National Laboratory for Physical Sciences at the Microscale, Collaborative Innovation Center of Chemistry for Energy Materials, School of Chemistry and Materials Science, University of Science and Technology of China, Hefei, China. [3]Department of Theoretical Chemistry and Biology School of Engineering Sciences in Chemistry, Biotechnology and Health, Royal Institute of Technology, Stockholm, Sweden. [4]Beijing National Laboratory for Condensed Matter Physics, Institute of Physics, Chinese Academy of Sciences, Beijing, China. [5]Department of Materials Science and Nano Engineering, Rice University, Houston, TX, USA. [6]These authors contributed equally: Daobin Liu, Xiyu Li. *e-mail: jiangj1@ustc.edu.cn; song2012@ustc.edu.cn

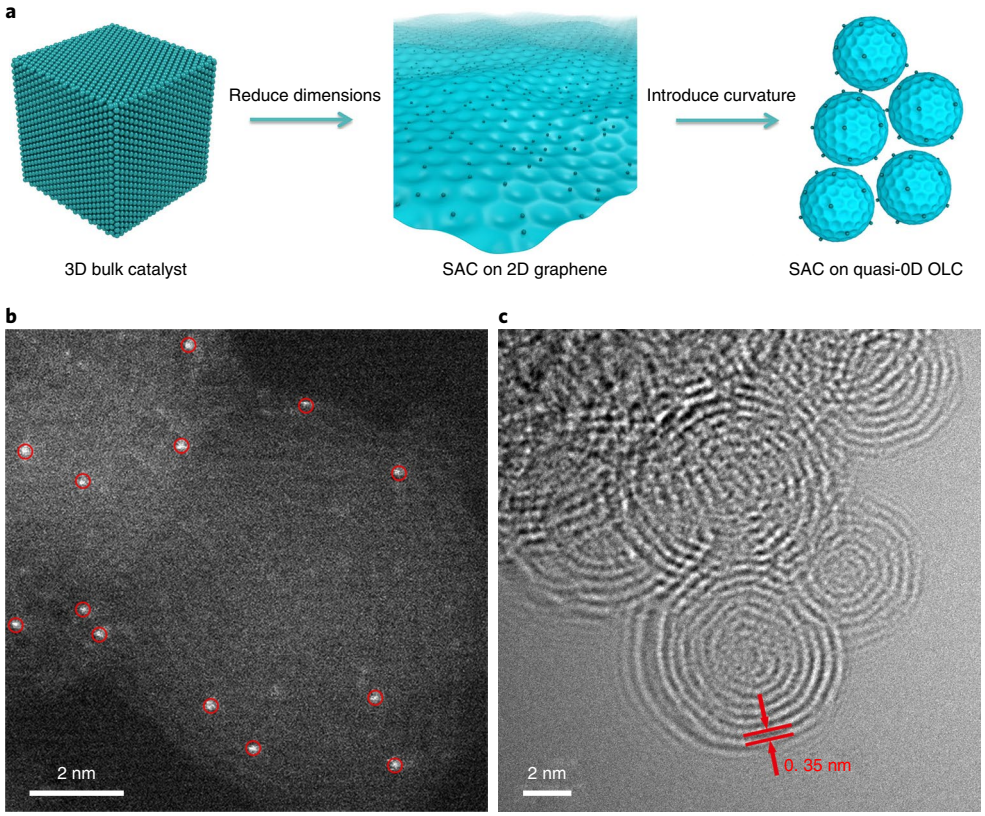

Fig. 1 | Rational design of the Pt_1/OLC catalyst via reducing the dimensions and introducing curvature. a, The schematic illustrates the approach taken in this work, whereby catalytically active particles were reduced in size to a single-atom form and the dimensionality of the catalyst support was reduced by using quasi-0D OLCs. **b**, The HAADF-STEM image of Pt_1/OLC clearly displays the Pt single atoms (highlighted by red circles) randomly dispersed on the OLC supports. **c**, Transmission electron microscopy image of Pt_1/OLC shows a multishell fullerene structure with a layer distance of 0.35 nm.

of 0.35 nm were seen as OLC particles after annealing the oxidized DND at 1,500 °C (Fig. 1c)[21]. In contrast to the isolated Pt distribution, numerous Pt aggregates were seen if the support was treated at low temperatures or reoxidized after the 1,500 °C heat treatment (Supplementary Fig. 4), which suggests an important role of the oxygen functionalities on the supports to obtain a single-metal atom distribution after ALD metal deposition. The Pt-loading contents were extracted by inductively coupled plasma atomic emission spectroscopy (ICP-AES), as summarized in Supplementary Table 1. The as-prepared Pt_1/OLCs have a low Pt content of 0.27 wt%. To obtain a deeper insight on the Pt loadings, X-ray photoelectron spectroscopy (XPS) was used to probe the surface chemical environment of oxygen on the supports. Notably, the Pt loading content was positively related to the density of the oxygen species (Supplementary Table 1) and it was identified that the phenolic oxygen[22] became the dominant oxygen species for higher temperature heat-treated OLCs (Supplementary Fig. 2), which then largely contributes in attracting Pt precursors (trimethyl(methylcyclopentadienyl)platinum(IV) ($MeCpPtMe_3$)). This triggers in situ coordination reactions, which subsequently stabilize metal atoms by forming Pt–O bonds.

Structural identification

To capture more information about the atomic coordination and structural signature, the extended X-ray absorption fine structure (EXAFS) measurements were carried out on Pt_1/OLC samples[23]. Figure 2a shows the k^3-weighted Fourier transform (FT) curves at R space of Pt L_3 edge EXAFS spectra for Pt_1/OLC in comparison with the references of PtO_2, Pt foil and Pt ligands/OLC (which was collected by performing the $MeCpPtMe_3$ pulse step only, without O_3 exposure). The peak at 1.67 Å for Pt_1/OLC is similar to that of PtO_2 and corresponds to Pt–C/O bonds, while the spectra features of Pt_1/OLC are significantly distinct from that of the Pt foil (metal), showing no appearance of larger Pt aggregates. Specifically, the 1.67 Å peak of Pt_1/OLC increases in intensity and shifts up in contrast to the Pt ligands/OLC, which can be ascribed to the additional formation of Pt–O bonds after O_3 exposure. It is further validated by the fitting results shown in Supplementary Fig. 5 and Supplementary Table 2[24]. The Pt single atoms on the OLC support were stabilized by one carbon atom and two oxygen atoms ($Pt_1O_2C_1$). To confirm the oxidation state of the isolated Pt atoms in Pt_1/OLC, X-ray absorption near-edge structure (XANES) spectra (Fig. 2b) were also collected. The various intensities of white line peaks correspond to electronic transitions from $2p_{3/2}$ to unoccupied 5*d* states[25]. It shows that the dominant features of Pt_1/OLC are situated between the Pt foil (Pt^0) and PtO_2 (Pt^{IV}), which indicates a cationic environment. Furthermore, deconvolution of the Pt 4*f* XPS spectrum (Fig. 2c) exhibits a single doublet ($4f_{7/2}$ and $4f_{5/2}$) at 73.3 and 76.6 eV, which can be attributed to the presence of the Pt^{II} oxidation state in Pt_1/OLC[26]. The corresponding survey and deconvoluted C 1*s* spectra of Pt_1/OLC are also shown in Supplementary Fig. 6.

Based on the geometric details identified by the above experiments, atomic models can be proposed for a first-principles examination with density functional theory (DFT). The model of PtO_2C_{295} was constructed by encapsulating a C_{60} fullerene within a defective fullerene of C_{235}, in which a Pt atom is bonded to a surface C atom and two O atoms (Fig. 2d). The optimized bond lengths of Pt–O and Pt–C are in good agreement with the EXAFS data. Importantly, the anchored Pt atom sticks out from the curved surface of the spherical

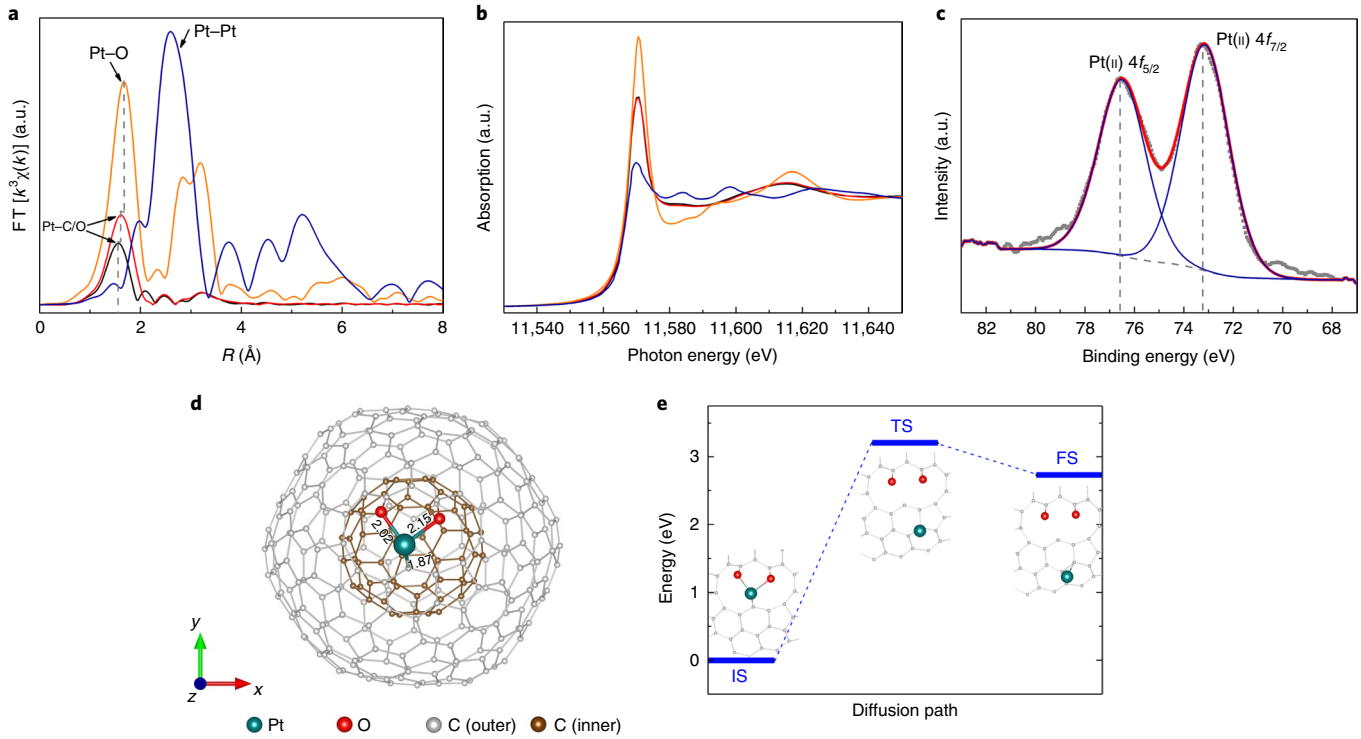

Fig. 2 | Structural identification of Pt single atom in Pt_1/OLC catalyst. a,**b**, The Pt L_3 edge FT-EXAFS spectra of Pt_1/OLC (red), along with PtO_2 (yellow), Pt foil (blue) and the Pt ligands/OLC (black) (without O_3 exposure to remove their ligands in $MeCpPtMe_3$ precursors) for comparison (**a**) and the corresponding normalized XANES spectra (**b**). **c**, High-resolution XPS Pt 4*f* spectrum of Pt_1/OLC, where it is fitted by fixing the spin–orbit splitting of 3.3 eV and area ratio of 4:3 for a doublet pair ($4f_{7/2}$ and $4f_{5/2}$). **d**, The optimized atomic model of PtO_2C_{295}, which exhibits Pt–O bonding in accordance with the experiments, where the grey and brown balls represent the carbon atoms in the outer/inner shell of fullerene-like structure. **e**, The lowest diffusion barrier (most probable diffusion path) of a Pt atom on PtO_2C_{295} is as high as 3.2 eV, which demonstrates the stability of Pt anchoring. IS, initial state; TS, transition state; FS, final state. a.u., arbitrary units.

fullerene structure. The diffusion of Pt on the PtO_2C_{295} surface needs to overcome a high energy barrier of 3.20 eV, which indicates an excellent structural stability for this arrangement (Fig. 2e). In sharp contrast, the system of Pt supported by C_{300} without Pt–O binding shows a low diffusion barrier (0.75 eV) and poor stability (Supplementary Fig. 7).

Electrochemical HER performance

To demonstrate the facilitation of catalytic reactions that arises from the combination of Pt single atoms and curved OLC supports, as-obtained samples were evaluated for hydrogen evolution by the rotating disk electrode (RDE) technique with a three-electrode configuration in N_2-saturated 0.5 M H_2SO_4 electrolytes (Supplementary Fig. 8). As expected, the Pt-metal-based catalysts have negligible onset potentials near the thermodynamic potential of the HER (Fig. 3a). The Pt_1/OLC with only 0.27 wt% of Pt achieved a very low overpotential (η) of ~38 mV at a current density of 10 mA cm^{-2}, which is comparable to that of a commercial Pt/C catalyst with a 20 wt% Pt loading and much better than that of a 5 wt% Pt loaded Pt/C catalyst (Supplementary Figs. 9 and 10). Furthermore, the atomically dispersed Pt supported on graphene (Pt_1/graphene, 0.33 wt% Pt (Supplementary Fig. 11)) was prepared by the same ALD procedure. It also exhibited an inferior performance even though the Pt loading was slightly higher than that of the Pt_1/OLC hybrid. Tafel plots were derived from the polarization curves to provide a deeper insight of the detailed mechanism of HER of Pt_1/OLC and the reference samples. The Tafel slope of 36 mV dec^{-1} for the Pt_1/OLC catalyst is close to that of 20 wt% Pt/C (35 mV dec^{-1}) (Fig. 3b). This illustrates that the Volmer–Tafel mechanism dominates in the HER process, where the recombination of adsorbed H* is the rate-determining step[6]. Further, electrochemical impedance spectroscopy was applied to investigate the electrode kinetics for proton reduction under polarization at η of 30 mV. The Nyquist plots in Supplementary Fig. 12 show that the Pt_1/OLC has an extremely low charge transfer resistance (R_{ct}) of 6.88 Ω, implying a fast Faradaic process at the interface between the catalyst and electrolyte. Besides, the Nyquist plot of the Pt_1/OLC catalyst collected at an η of 0 mV shows a low equivalent series resistance and is almost vertical at low frequencies, which implies an ideal capacitive behaviour of the OLC supports (Supplementary Fig. 13a)[27]. The relaxation time from the Nyquist plot is only 56 ms for the Pt_1/OLC catalyst, being much faster than any other control catalysts. This suggests that this quasi-0D system has a fully accessible surface in the electrolyte, which favours an increased ability to transfer the ion (H^+) reactant (Supplementary Fig. 13b–e)[21].

Figure 3c shows the comparison of mass activity that normalized all the samples to the Pt loading at the same overpotential ($\eta = 38$ mV). The Pt_1/OLC catalyst (7.40 A mg^{-1}_{Pt}) can achieve a mass activity ~2.5 times higher than that of the Pt_1/graphene catalyst (2.82 A mg^{-1}_{Pt}), and ~43 times higher than those of the reference commercial Pt/C catalysts (0.17 A mg^{-1}_{Pt}). Owing to the uniformly distributed Pt single atoms on carbon supports, the active site density (sites cm^{-2}) can be estimated based on the total electrochemical active surface area (ECSA) that is proportional to the double-layer capacitance (C_{dl}) of the electrode surface (Supplementary Fig. 14)[28]. The value of 5.8×10^{13} sites cm^{-2} for Pt_1/OLC is approximately identical to that of Pt_1/graphene (5.9×10^{13} sites cm^{-2}), which suggests that the difference in number of active sites is not a primary reason for the higher catalytic performance of Pt_1/OLC. Thereafter, we calculated the turnover frequency (TOF) to quantify the catalytic

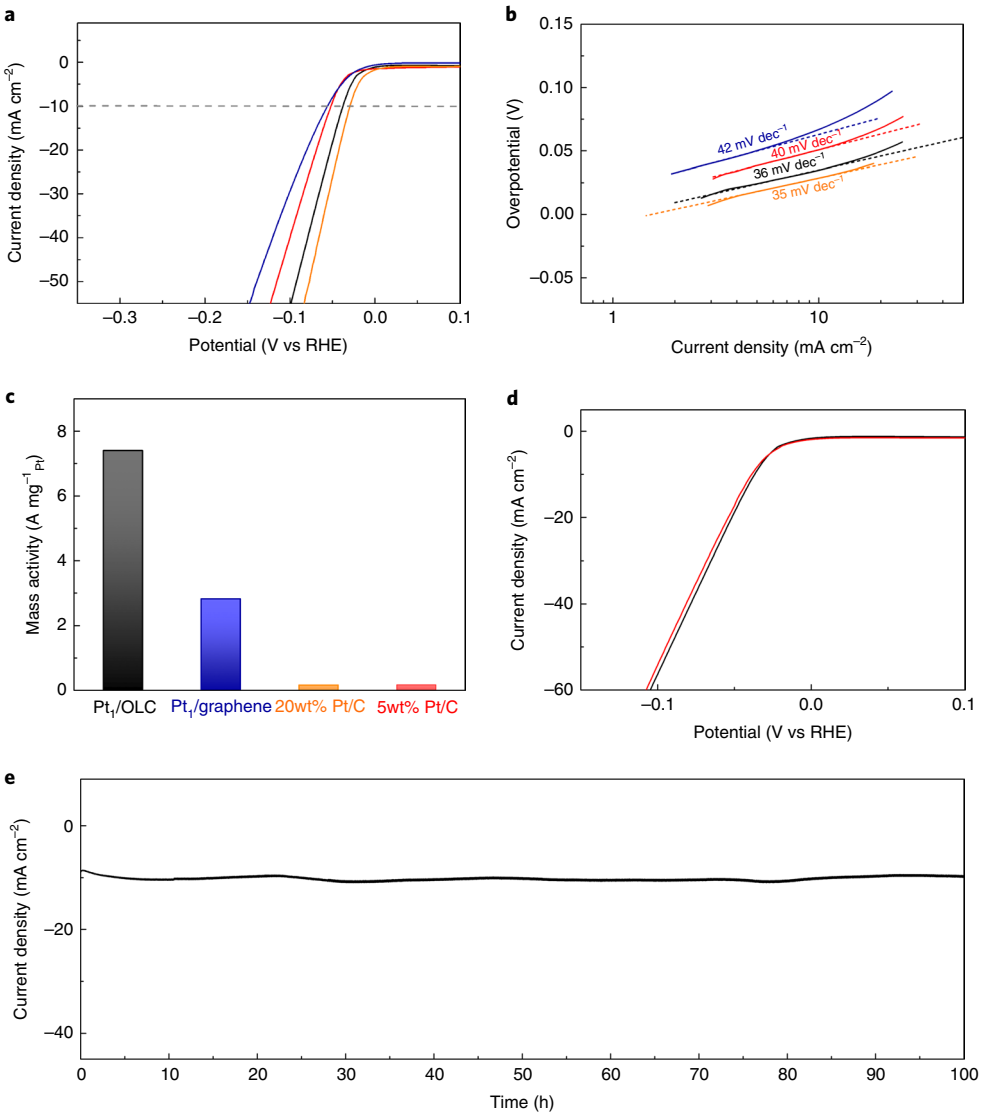

Fig. 3 | Hydrogen evolution performance of the Pt_1/OLC catalyst. a, Polarization curves of Pt_1/OLC (black) in comparison with 5 wt% and 20 wt% commercial Pt/C (red and orange, respectively) and Pt_1/graphene (0.33%) (blue) in a 0.5 M H_2SO_4 electrolyte. The catalyst loading calculated by total weight is 510 μg cm^{-2} for all the catalysts. **b**, Tafel plots derived from the corresponding polarization curves. **c**, The mass activity of Pt_1/OLC is normalized to the Pt loading at an η of 38 mV with respect to the reference catalysts. **d**, Polarization curves for an accelerating stability measurement in 0.5 M H_2SO_4 were recorded before (black) and after (red) 6,000 CV sweeps in the range of −0.05 V to 0.2 V at a scan rate of 50 mV s^{-1}. **e**, The time-dependent current density curve of Pt_1/OLC was obtained at a constant overpotential of $\eta = 40$ mV for 100 h under acidic conditions (0.5 M H_2SO_4).

efficiency of each Pt site. As shown in Supplementary Fig. 15, the TOF values of the Pt SACs are significantly higher than those of most HER catalysts at various overpotentials, especially the recently reported atomic metal species supported on carbon supports[28,29]. Of note, the TOF can approach as high as 40.78 H_2 s^{-1} at an η of 100 mV for Pt_1/OLC, whereas the Pt_1/graphene catalyst has a TOF of 17.67 H_2 s^{-1}. These results imply that the excellent catalytic performance of Pt_1/OLC can be ascribed to the full utilization of Pt species and their unique local structure on the quasi-0D OLC supports.

To assess the durability of the as-proposed Pt_1/OLC catalyst, polarization curves were collected after 6,000 cyclic voltammetry (CV) sweeps and revealed only a small shift in potential at the same current density as the initial curve (Fig. 3d). HAADF-STEM and XPS results further confirmed that there was no noticeable change in atomic Pt dispersion and chemical states even after long cycling reactions (Supplementary Fig. 16). Moreover, the amperometric current density–time response shows that the as-prepared Pt_1/OLC electrode is maintained at a current density of 10 mA cm^{-2} for more than 100 hours without any detectable loss (Fig. 3e). This demonstrates the robust stability of Pt_1/OLC in acidic medium, which we suggest is due to the strong interaction between the Pt single atom and the OLC supports through the interfacial oxygen species.

To shed light on the working mechanism of the Pt_1/OLC catalyst, we simulated the electrocatalytic HER at the DFT level with the PtO_2C_{295} model extracted from XAFS results. Based on the computational hydrogen evolution model (with pH = 0 from the experiment)[30], we simulated the HER at the equilibrium potential. With a constant potential of $U = 0$, the state-of-the-art constant potential algorithm with grand canonical DFT[31] calculations, as implemented in the JDFTx code (Methods gives details)[32], was applied. The calculated free energy changes (ΔG) (ref. [33]) for the first and second adsorbed hydrogen atoms were found to be −0.92 and −0.50 eV, respectively (Fig. 4a and Supplementary Fig. 17), which suggests strong absorptions of hydrogen on the unsaturated coordinate of Pt.

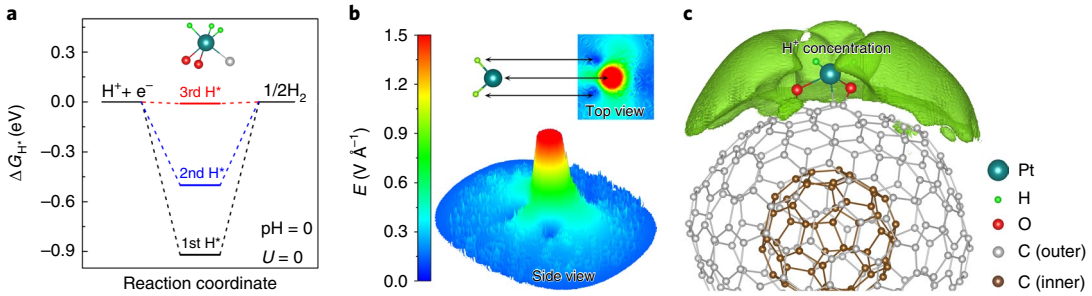

Fig. 4 | Theoretical investigation of the HER using the Pt_1/OLC catalyst. a, Calculated free-energy diagram of the HER at the equilibrium potential with pH = 0 and assuming that Pt is the active site. The inset shows the model of H adsorbed on the Pt site, where light green, green, red and grey balls represent, respectively, hydrogen, platinum, oxygen and carbon atoms. **b**, The map of the electric field shows a localized electric field of the H_2Pt_1/OLC system at the tip-like Pt site with an equilibrium potential. **c**, Based on the Gouy–Chapman–Stern model, a high concentration of protons (>1.99 mol l^{-1}) is distributed around the Pt site (represented by the green shape), which is induced by the local electric field at the Pt site. The grey carbon atoms consist of the outer fullerene-like structure of OLC, whereas the brown carbon atoms represent the inner shell.

That is, the HER activities are quite low when the Pt_1/OLC catalyst is clean or with only one hydrogen adsorbed on it. In contrast, the calculated ΔG becomes −0.01 eV for the third hydrogen adsorption. It is well known that the ΔG of an ideal HER catalyst is zero. From these results, we suggest that the catalyst that forms in situ may be H_2Pt_1/OLC.

The effective mass transfer of protons to the active Pt site is another key factor that determines hydrogen evolution activity. Our calculations suggest that an in situ strong local electric field around the Pt site at an equilibrium potential forms (Fig. 4b) and protrudes out of the curved OLC surface like a tip. Recently, a similar tip effect was found to promote the electrocatalysis of CO_2 reduction by causing a localized electric field and high reactant concentration around the active sites[34,35]. Using the Gouy–Chapman–Stern model to explore the distribution of the proton (H^+) reactant density in the PtO_2C_{295} (ref. [36]), we identified a remarkable enrichment of protons (>1.99 mol l^{-1}) around Pt (Fig. 4c), which could improve the proton mass transfer for the subsequent HER[35]. In sharp contrast, no comparable effects of a strong local electric field and high local proton concentration near the surface were found in the configuration of OLC (C_{300}) without Pt present (Supplementary Fig. 18).

Conclusions

Compared to the conventional bulk or graphene-supported Pt catalysts, we propose that nanoscale OLC particles with a curved nature enable the integration of an efficient charge delivery and a strong local electric field effect for Pt_1/OLC electrocatalysts. The optimized electrocatalyst, using only 0.27 wt% Pt to achieve a comparable HER rate to that of the commercial Pt/C catalyst (20 wt% Pt) and a better rate than that of graphene-supported catalyst with a similar Pt loading, represents a significant advancement in developing high-performance supported catalysts by the engineering of single metal atoms on nanoscale carbon supports. Computational modelling suggests that a tip-enhancement effect at the Pt site that extracts localized electrons from the support and induces strong localized electric fields may be a factor in enhancing the activity for HER.

Methods

The synthesis of Pt_1/OLC. Two main synthesis processes were involved in the preparation of the catalyst: a thermal annealing method was used to prepare the OLC and tune the density of the oxygen species and an ALD technique was used to deposit Pt precursors on the OLC supports. Typically, pristine DND powder (Henan Union Abrasive Co. Ltd) was first oxidized to remove the amorphous carbon and graft the oxygen functional groups outside the surface. The pristine DND powder (1 g) was added to a 100 ml mixture of H_2SO_4 and HNO_3 (3:1 volume ratio) and refluxed at 160 °C for 24 h (ref. [37]). When cooled down, the oxidized DND was washed with deionized water several times until a pH value of 7 was achieved, followed by lyophilization to dry it. To tune the density of the oxygen species, the obtained powder was treated by thermal deoxygenation at different temperatures under an Ar atmosphere. To prepare the reoxidized OLC supports, the OLC 1,500 °C hybrid was oxidized by HNO_3 at 80 °C for 4 h. Deposition of Pt atoms onto the OLC 1,500 °C support was carried out on a viscous flow reactor (GEMSTAR-6TM Benchtop ALD, Arradiance) and the Pt ALD cycle was performed at 150 °C using the $MeCpPtMe_3$ precursor (99.9%, Sigma Aldrich) and O_3. Ultrahigh purity N_2 (99.999%) was used as the carrier gas at a flow rate of 200 ml min^{-1}. The precursor container was heated to 65 °C to obtain a sufficient vapour pressure. The chamber was heated to 150 °C and the manifold was held at 110 °C to avoid the precursor condensation. The timing sequence was 40, 120, 120 and 120 s for $MeCpPtMe_3$ exposure, N_2 purge, O_3 exposure and N_2 purge, respectively. Note that, for comparison, the same ALD procedure was used for other obtained support materials deoxygenated at different conditions.

The synthesis of Pt_1/graphene. Graphene oxide was prepared by the improved method according to the previous report[38]. In brief, a mixture of 120 ml of concentrated H_2SO_4 and 14 ml of H_3PO_4 was added to graphite flakes (1.0 g), then the temperature was held at around 35–40 °C and 6 g of $KMnO_4$ was slowly added to it. The reaction was carried out at 50 °C and stirred for 12 h. When cooled down, ice along with several drops of 30 wt% H_2O_2 were poured in until the solution turned yellow. The precipitates were filtered out and washed using 300 ml of 5 wt% HCl three times, followed by deionized water several times until a pH value of 7 was attained. The final products were freeze-dried. The as-prepared graphene oxide nanosheets were annealed at 1,050 °C for 10 min under an Ar atmosphere and served as a loading support to the anchored Pt atoms. We carried out a one-cycle ALD procedure using the same timing sequence as that for Pt_1/OLC.

Material characterizations. Transmission electron microscopy was performed on a JEM-2100F field-emission microscope (JEOL Ltd) operated at an accelerating voltage of 200 kV, and aberration-corrected STEM images were taken using a 200 kV JEM-ARM200F equipped with double spherical aberration correctors. The PerkinElmer Optima 7300 DV ICP-AES instrument was used to determine the content of Pt loading after digesting the powdered sample in HNO_3. XPS measurements were carried out on a Thermal VG Scientific ESCALAB250 spectrometer equipped with an Al anode (Al Kα = 1,486.7 eV). All the spectra were corrected with respect to the C 1*s* peak at 284.8 eV. The XPSPEAK 4.1 software was used for the deconvolution of XPS spectra. X-ray diffraction patterns were recorded by using a Rigaku Smartlab instruments equipped with Cu Kα radiation (λ = 1.54178 Å). Raman spectra were performed on a Horiba LabRamHR system combined with a 325 nm laser.

XAFS measurements and simulations. Synchrotron radiation-based XAFS is known as a powerful element-specific tool to study the local structure around selected elements that are contained within a material. XANES is the measurement of the X-ray absorption coefficient of a material as a function of energy, typically in a 50–100 eV range that begins before the absorption edge of a given element in the sample. The Pt L_3 edge XAFS spectra were collected at the beamline 14W1 in the Shanghai Synchrotron Radiation Facility, a 3.5 GeV third-generation synchrotron source, using a Si(111) double-crystal monochromator in transmission mode. The energy position was calibrated with a Pt foil. The raw absorption data were first background subtracted by fitting the pre-edge using a least-squares method, and then normalized to one at energies far from the edge. All the spectra were processed using the WinXAS version 3.1 Program[24]. Simulations of the EXAFS scattering paths to fit experimental data were

calculated with the FEFF8.2 code[39] using the crystal structural parameters of the Pt foil and PtO_2.

Electrochemical measurements. To fabricate the working electrode, 5 mg of each catalyst with 50 µl of 5 wt% Nafion solution (Sigma-Aldrich) was dispersed in 1 ml of a water/isopropanol mixed solvent (1:1 volume ratio) by several hours of sonication to form a homogeneous ink. A glassy carbon disk served as the working electrode to drop the catalyst ink on the surface, which resulted in a catalyst loading of 510 µg cm^{-2} (calculated by the total weight) for all electrochemical tests. Note that the glassy carbon disk electrode of the RDE is 5 mm in diameter, whereas a rotating ring-disk electrode (RRDE) electrode (which contains a Pt ring with a 6.25 mm inner diameter and 7.92 mm outer diameter) is 5.61 mm in diameter.

The electrochemical measurements were carried out on a CHI 660E workstation (the RRDE measurement was performed with an Autolab PGSTAT 302N potentiostat) with a rotation control (MSR (Pine Instruments)) using a conventional three-electrode cell in 0.5 M H_2SO_4 at room temperature. For the counter electrode, a graphite rod was used. An Ag/AgCl electrode (saturated KCl) was used as the reference electrode, which was calibrated with respect to the reversible hydrogen electrode (RHE) under the high purity hydrogen-saturated electrolyte with a Pt mesh as the working electrode (Supplementary Fig. 8)[40]. The RDE/RRDE measurements were performed in N_2-saturated electrolyte at 2,000 revolutions per minute with a sweep rate of 5 mV s^{-1} to remove the generated gas bubbles. To detect the hydrogen evolution at the disk electrode, the potential of the Pt ring electrode in the RRDE system was set to 1.2 V (versus RHE). Electrochemical impedance spectroscopy measurements were carried out at an overpotential of $\eta = 0$ mV or 30 mV, with a 5 mV a.c. potential from 0.1 to 10^5 Hz. An accelerating stability measurement was evaluated using 6,000 continuous cycles from −0.05 to 0.2 V (versus RHE) at a scan rate of 50 mV s^{-1}. The time-dependent current density curve was collected by loading catalyst ink onto carbon paper (1 cm × 1 cm TGP-H-60 (Toray)) and the overpotential maintained at an η of 40 mV for 100 h.

TOF and active-site density calculations. The TOF and active-site density[28] were estimated based on the assumption that all the single atoms of Pt (determined by the ICP-AES results) were exposed.

The active-site density of single-atom Pt catalysts can be estimated from the number of isolated Pt atoms and the total ECSA of the electrode, because Pt species in the isolated form were randomly distributed on the surface of carbon supports.

$$\text{Density of Pt sites} = \frac{\text{Number of Pt active sites}}{\text{ECSA of the electrode}}$$

The number of Pt active sites loading on the electrode can be calculated from the total mass loading of the catalyst, the content of Pt and the Pt atomic weight, according to the equation:

$$\text{Number of Pt active sites} = \left(\frac{\text{Catalyst loading on the electrode (g cm}^{-2}) \times \text{Pt content (wt\%)}}{\text{Pt atomic weight (g mol}^{-1})}\right)\left(\frac{6.022\times10^{23}\ \text{Pt}}{1\ \text{mol Pt}}\right)$$

The ECSA of the electrode was determined by the electrochemical double-layer capacitance (C_{dl}), using CV at a different scan rate in the non-Faradaic region as shown in Supplementary Fig. 14. Moreover, the specific capacitance (C_s) for a flat surface is generally found to be in the range of 20–60 µF cm^{-2}. We used a value of 40 µF cm^{-2} in this work:

$$\text{ECSA of the electrode} = \frac{C_{dl}}{C_s}$$

TOF is defined as the number of H_2 evolved on an active site per second. Here, we calculated according to the following equations:

$$\text{TOF} = \frac{\text{Total hydrogen turnovers per geometric area}}{\text{The number of Pt active sites}}$$

The total number of hydrogen turnovers was calculated from the linear sweep voltammetry curve according to:

$$\text{Total hydrogen turnovers} = (|j|\ \text{mA cm}^{-2})\left(\frac{1\ \text{C s}^{-1}}{1{,}000\ \text{mA}}\right)\left(\frac{1\ \text{mol } e^-}{96485.3\ \text{C}}\right)\left(\frac{1\ \text{mol}}{2\ \text{mol } e^-}\right)\left(\frac{6.022\times10^{23}\ \text{molecules H}_2}{1\ \text{mol H}_2}\right)$$

$$= 3.12\times10^{15}\ |j|\ \frac{\text{H}_2\ \text{s}^{-1}}{1\ \text{cm}^2}\ \text{per mA cm}^{-2}$$

where e^- means electrons. Thus, the current density from the linear sweep voltammetry curve can be converted into TOF values as follows:

$$\text{TOF} = \frac{3.12\times10^{15}}{\text{Number of Pt active sites}} \times |j|$$

Theoretical calculations. To examine the stability of this catalytic system, the climbing image nudged elastic band method was used to calculate the diffuse barrier of the Pt atom of Pt_1/OLC. The calculations of atomic and electronic structures of the PtO_2C_{295} catalyst were performed using the Vienna Ab-initio Simulation Package at the spin-polarized DFT level[41]. The Perdew–Burke–Ernzerhof functional for the exchange correlation term was used with the projector augmented wave method[42] and a cutoff energy of 500 eV. The model of the OLC consists of a C_{60} encapsulated by C_{240} in a vacuum box with sides $a = b = c = 25$ Å. Based on the experimental results of the EXAFS spectra, we constructed the atomic structure of Pt_1/OLC, shown in Fig. 2d. A 1 × 1 × 1 Monkhorst–Pack k-point sampling was used for all the calculations. All the structures were fully relaxed to the ground state and spin polarization was considered. The convergence criteria of the energy and forces were set to 1×10^{-5} eV and 0.02 eV Å^{-1}, respectively. Based on the method of computational hydrogen evolution, we used grand canonical DFT[31] as implemented in the JDFTx[32] code to calculate the free energy change of the hydrogen absorption reaction at the equilibrium potential[36]. The hydrogen-adsorbed structures were relaxed with an energy cutoff of 20 Hartrees as calculated with the Perdew–Becke–Erzenhof exchange-correlation functional. The CANDEL[43] implicit solvation model was used. The structures were fully relaxed until the final force on each atom was less than 0.01 eV Å^{-1}. The free energy of a system is obtained by adding the vibrational contribution of the adsorbate to the electronic energy of the system[44].

The details for the method of calculation of ΔG at the HER equilibrium potential ($U = 0$) takes account of both the charge effect and the solvation effect[32].

When considering both the charge effect and the solvation effect during HER, ΔG becomes:

$$\Delta G_{cpm} = G_{sol}(\text{H}^{*Q_2}) - G_{sol}(^{*Q_1}) - G(\text{H}_2(\text{g}))/2 + |e|\ U - (Q_1 - Q_2)\mu_e \quad (1)$$

where * represents the catalyst, e is the elementary charge, U is the applied electrode potential with respect to the RHE, μ_e is the electron energy defined by the absolute electrode potential. Q_1 and Q_2 are the net charges on the catalyst before and after H adsorption, which are determined by the constraint:

$$E_F(^{*Q_1}) = E_F(\text{H}^{*Q_2}) = \mu_e \quad (2)$$

and thus are U dependent. The subscript 'cpm' emphasizes that the E_F (Fermi energy) level is fixed during the reaction and the subscript 'sol' indicates that the system is embedded in a solution that can balance the extra charge on the catalyst by the counterions. Here, the computational hydrogen evolution model was adopted to consider the free energy of the $(H^+(aq) + e^-)$ couple. As the experimental pH is zero, we set μ_e to 4.6 eV in our calculations.

Data availability

The data that support the plots within this paper and other findings of this study are available from the corresponding author upon reasonable request

Received: 25 December 2017; Accepted: 29 April 2019;
Published online: 03 June 2019

References

1. Seh, Z. W. et al. Combining theory and experiment in electrocatalysis: insights into materials design. *Science* **355**, eaad4998 (2017).
2. Greeley, J., Jaramillo, T. F., Bonde, J., Chorkendorff, I. B. & Norskov, J. K. Computational high-throughput screening of electrocatalytic materials for hydrogen evolution. *Nat. Mater.* **5**, 909–913 (2006).
3. Deng, D. et al. Catalysis with two-dimensional materials and their heterostructures. *Nat. Nanotechnol.* **11**, 218–230 (2016).
4. Nilsson, A. et al. The electronic structure effect in heterogeneous catalysis. *Catal. Lett.* **100**, 111–114 (2005).
5. Yin, Y. et al. Contributions of phase, sulfur vacancies, and edges to the hydrogen evolution reaction catalytic activity of porous molybdenum disulfide nanosheets. *J. Am. Chem. Soc.* **138**, 7965–7972 (2016).
6. Jiao, Y., Zheng, Y., Davey, K. & Qiao, S. Z. Activity origin and catalyst design principles for electrocatalytic hydrogen evolution on heteroatom-doped graphene. *Nat. Energy* **1**, 16130 (2016).
7. Liu, P. et al. Photochemical route for synthesizing atomically dispersed palladium catalysts. *Science* **352**, 797–801 (2016).
8. Qiao, B. et al. Single-atom catalysis of CO oxidation using Pt_1/FeO_x. *Nat. Chem.* **3**, 634–641 (2011).

9. Yan, H. et al. Single-atom Pd_1/graphene catalyst achieved by atomic layer deposition: remarkable performance in selective hydrogenation of 1,3-butadiene. *J. Am. Chem. Soc.* **137**, 10484–10487 (2015).
10. Liu, G. et al. MoS_2 monolayer catalyst doped with isolated Co atoms for the hydrodeoxygenation reaction. *Nat. Chem.* **9**, 810–816 (2017).
11. Thomas, J. M. Catalysis: tens of thousands of atoms replaced by one. *Nature* **525**, 325–326 (2015).
12. Yang, X. F. et al. Single-atom catalysts: a new frontier in heterogeneous catalysis. *Acc. Chem. Res.* **46**, 1740–1748 (2013).
13. Bayatsarmadi, B., Zheng, Y., Vasileff, A. & Qiao, S. Z. Recent advances in atomic metal doping of carbon-based nanomaterials for energy conversion. *Small* **13**, 1700191 (2017).
14. Mahmood, J. et al. An efficient and pH-universal ruthenium-based catalyst for the hydrogen evolution reaction. *Nat. Nanotechnol.* **12**, 441–446 (2017).
15. Cheng, N. et al. Platinum single-atom and cluster catalysis of the hydrogen evolution reaction. *Nat. Commun.* **7**, 13638 (2016).
16. Tiwari, J. N. et al. Multicomponent electrocatalyst with ultralow Pt loading and high hydrogen evolution activity. *Nat. Energy* **3**, 773–782 (2018).
17. Yin, X. P. et al. Engineering the coordination environment of single-atom platinum anchored on graphdiyne for optimizing electrocatalytic hydrogen evolution. *Angew. Chem. Int. Ed.* **57**, 9382–9386 (2018).
18. Kwak, J. H. et al. Coordinatively unsaturated Al^{3+} centers as binding sites for active catalyst phases of platinum on γ-Al_2O_3. *Science* **325**, 1670–1673 (2009).
19. Yang, M. et al. A common single-site Pt(II)–$O(OH)_x$-species stabilized by sodium on 'active' and 'inert' supports catalyzes the water–gas shift reaction. *J. Am. Chem. Soc.* **137**, 3470–3473 (2015).
20. Zeiger, M., Jäckel, N., Mochalin, V. N. & Presser, V. Review: carbon onions for electrochemical energy storage. *J. Mater. Chem. A* **4**, 3172–3196 (2016).
21. Pech, D. et al. Ultrahigh-power micrometre-sized supercapacitors based on onion-like carbon. *Nat. Nanotechnol.* **5**, 651–654 (2010).
22. Ganguly, A., Sharma, S., Papakonstantinou, P. & Hamilton, J. Probing the thermal deoxygenation of graphene oxide using high-resolution in situ X-ray-based spectroscopies. *J. Phys. Chem. C* **115**, 17009–17019 (2011).
23. Sun, Z., Liu, Q., Yao, T., Yan, W. & Wei, S. X-ray absorption fine structure spectroscopy in nanomaterials. *Sci. China Mater.* **58**, 313–341 (2015).
24. Ressler, T. WinXAS: a program for X-ray absorption spectroscopy data analysis under MS-windows. *J. Synchrotron Radiat.* **5**, 118–122 (1998).
25. Yoshida, H., Nonoyama, S., Yazawa, Y. & Hattori, T. Quantitative determination of platinum oxidation state by XANES analysis. *Phys. Scr.* **T115**, 813–815 (2005).
26. Li, Y. et al. Implementing metal-to-ligand charge transfer in organic semiconductor for improved visible-near-infrared photocatalysis. *Adv. Mater.* **28**, 6959–6965 (2016).
27. Rennie, A. J., Sanchez-Ramirez, N., Torresi, R. M. & Hall, P. J. Ether-bond-containing ionic liquids as supercapacitor electrolytes. *J. Phys. Chem. Lett.* **4**, 2970–2974 (2013).
28. Fei, H. et al. Atomic cobalt on nitrogen-doped graphene for hydrogen generation. *Nat. Commun.* **6**, 8668 (2015).
29. Zhang, L. et al. Graphene defects trap atomic Ni species for hydrogen and oxygen evolution reactions. *Chem* **4**, 285–297 (2018).
30. Nørskov, J. K. et al. Trends in the exchange current for hydrogen evolution. *J. Electrochem. Soc.* **152**, J23–J26 (2005).
31. Sundararaman, R., Goddard, W. A. & Arias, T. A. Grand canonical electronic density-functional theory: algorithms and applications to electrochemistry. *J. Chem. Phys.* **146**, 114104 (2017).
32. Sundararaman, R. et al. JDFTx: software for joint density-functional theory. *SoftwareX* **6**, 278–284 (2017).
33. Kim, D., Shi, J. & Liu, Y. Substantial impact of charge on electrochemical reactions of two-dimensional materials. *J. Am. Chem. Soc.* **140**, 9127–9131 (2018).
34. Liu, M. et al. Enhanced electrocatalytic CO_2 reduction via field-induced reagent concentration. *Nature* **537**, 382–386 (2016).
35. Jiang, H., Hou, Z. & Luo, Y. Unraveling the mechanism for the sharp-tip enhanced electrocatalytic carbon dioxide reduction: the kinetics decide. *Angew. Chem. Int. Ed.* **56**, 15617–15621 (2017).
36. Oldham, K. B. A Gouy–Chapman–Stern model of the double layer at a (metal)/(ionic liquid) interface. *J. Electroanal. Chem.* **613**, 131–138 (2008).
37. Haleem, Y. A. et al. Surface functionalization and structure characterizations of nanodiamond and its epoxy based nanocomposites. *Composites B* **78**, 480–487 (2015).
38. Marcano, D. C. et al. Improved synthesis of graphene oxide. *ACS Nano* **4**, 4806–4814 (2010).
39. Ankudinov, A. L., Ravel, B., Rehr, J. J. & Conradson, S. D. Real-space multiple-scattering calculation and interpretation of X-ray-absorption near-edge structure. *Phys. Rev. B* **58**, 7565–7576 (1998).
40. Li, Y. et al. An oxygen reduction electrocatalyst based on carbon nanotube–graphene complexes. *Nat. Nanotechnol.* **7**, 394–400 (2012).
41. Kresse, G. & Furthmuller, J. Efficiency of ab-initio total energy calculations for metals and semiconductors using a plane-wave basis set. *Comput. Mater. Sci.* **6**, 15–50 (1996).
42. Perdew, J. P., Burke, K. & Ernzerhof, M. Generalized gradient approximation made simple. *Phys. Rev. Lett.* **77**, 3865–3868 (1996).
43. Sundararaman, R. & Goddard, W. A. The charge-asymmetric nonlocally determined local-electric (CANDLE) solvation model. *J. Chem. Phys.* **142**, 064107 (2015).
44. Hinnemann, B. et al. Biomimetic hydrogen evolution: MoS_2 nanoparticles as catalyst for hydrogen evolution. *J. Am. Chem. Soc.* **127**, 5308–5309 (2005).

Acknowledgements

This study was financially supported in part by the MOST (nos 2017YFA0303500 and 2018YFA0208603), the NSFC (nos 11574280, 11375198, U1532112, 91127042, 21790350, 21633006 and 21473166), the Recruitment Program of Global Experts and the CAS Hundred Talent Program and the Anhui Initiative in Quantum Information Technologies (AHY090200 and AHY090000). We thank the SSRF (14W1), the BSRF (1W1B and soft X-ray), the NSRL (photoemission, MCD and catalysis/surface science) and the USTC Center for Micro and Nanoscale Research and Fabrication for help with the characterization. We also thank Y. Liu and J. Shi for helpful discussions.

Author contributions

L.S. and J.J. conceived the research and designed the project. D.L. performed most of the experiments. X.L., S.D. and J.J. performed the simulations. S.C. contributed to the XAS measurements. H.Y. and J.L. contributed to the ALD preparation. B.G. contributed to the STEM characterizations. C. Wang, C. Wu and Y.A.H. partially contributed to experimental data. D.L., X.L., P.M.A., Y.L., J.J. and L.S. analysed the data and co-wrote the paper. All the authors discussed the results and commented on the manuscript.

Competing interests

The authors declare no competing interests.

Additional information

Supplementary information is available for this paper at https://doi.org/10.1038/s41560-019-0402-6.

Reprints and permissions information is available at www.nature.com/reprints.

Correspondence and requests for materials should be addressed to J.J. or L.S.

Publisher's note: Springer Nature remains neutral with regard to jurisdictional claims in published maps and institutional affiliations.